

Guided wave signal processing and image fusion for *in situ* damage localization in plates

Jennifer E. Michaels ^{*}, Thomas E. Michaels

School of Electrical and Computer Engineering, Georgia Institute of Technology, 777 Atlantic Drive NW, Atlanta, Georgia 30332-0250, USA

Received 20 September 2006; received in revised form 18 December 2006; accepted 20 February 2007

Available online 2 March 2007

Abstract

A spatially distributed array of single element piezoelectric transducers is considered for monitoring the integrity of plate-like structures over large areas. When these permanently attached transducers are driven with an impulsive excitation, broadband Lamb waves are generated and received signals are complex, typically containing multiple modes as well as many boundary reflections. The complexity of the signals, including dispersive effects, can be reduced by digital bandpass filtering, and changes in these filtered signals over time can be monitored to detect and localize damage. Results are reported here from an experimental study whereby artificial damage was introduced in an aluminum plate in the form of through holes drilled at various locations. Time shift averaging algorithms were applied to differential signals filtered at multiple frequencies, resulting in many images for the same structural state, and these images were fused to improve damage localization and background noise. Individual and fused images were analyzed to quantify their ability to localize damage. The results show the efficacy of the imaging method as well as the significant improvement resulting from image fusion.

© 2007 Elsevier B.V. All rights reserved.

Keywords: Ultrasonics; Structural health monitoring; Damage localization; Imaging

1. Introduction

The use of guided wave modes such as Lamb and Rayleigh waves is of considerable interest for both non-destructive evaluation (NDE) and structural health monitoring (SHM) due to the ability of such waves to travel long distances in structures of engineering importance. Alleyne and Cawley [1] performed a systematic numerical and experimental study of the interaction of various Lamb wave modes with notches, and concluded that Lamb waves could detect notches with depths much smaller than the wavelength. Gnosch et al. [2] used immersion angle beam transducers to generate multi-modal Lamb waves and studied their interaction with horizontal and vertical defects; theoretical stress distributions were used to explain why specific modes were sensitive to different defect geometries. Fromme and Sayir [3] and Chang and Mal [4] investigated the interaction of Lamb waves with rivet hole cracks and demonstrated their potential for detecting this type

^{*} Corresponding author. Tel.: +1 404 894 2994; fax: +1 404 894 4641.

E-mail address: jennifer.michaels@ece.gatech.edu (J.E. Michaels).

of defect. Rose [5] summarizes the use of guided waves for many applications, and discusses the issues involved in finding a particular mode and frequency to solve a specific inspection problem. The utility of guided waves is particularly evident from the many applications of long range inspection of piping where either access to the surface is limited by insulation or the pipe itself is inaccessible over most of its length [6–8].

More recently, guided waves have been investigated for SHM applications for which piezoelectric sensors are permanently attached to plate-like structures such as aircraft wing skins. Both rectangular and circular element geometries have been evaluated [9,10], where the omnidirectional characteristics of circular elements are well-suited for directionally uniform interrogation of a large area. Multiple discrete transducer elements can be arranged in various array configurations to better interrogate large areas. Giurgiutiu et al. [11] and Purekar et al. [12] have utilized spatially compact linear arrays with the ability to form sector-type beam-formed images. Wilcox [13] has investigated omnidirectional circular arrays, and associated signal processing algorithms have included dispersion compensation. Transducer elements can be arranged on the periphery of an area and various tomographic algorithms implemented to construct images [14–16]. All of these approaches require a fairly large number of array elements, ranging from as few as eight to upwards of 40, to obtain reasonable localization of damage.

An alternative configuration is to spatially distribute a very small number of circular transducers over a large area, resulting in a sparse array. Various algorithms can be implemented, typically on residual signals, to generate images of damage [17–19]. All of these *in situ* array-based methods utilize signals that are dominated by a single mode, and are usually narrow band. Broadband signals containing multiple modes are more difficult to interpret, but contain more information and are easier to generate experimentally. Various analysis schemes appropriate for broadband signals have been proposed to detect and localize damage based upon changes in waveforms [20–22].

For the work presented here, circular transducer elements are arranged in a spatially distributed array, and through transmission signals from all transmit–receive pairs are recorded using a broadband impulsive excitation. Signals are recorded before and after introduction of damage, and residual signals are calculated and analyzed. Multi-frequency information is effectively utilized by digital bandpass filtering of the broadband signals to create a set of bandlimited signals with different center frequencies. Imaging methods are then applied to the bandlimited signals, generating a set of images corresponding to each center frequency. These images are then combined, or fused, to obtain a better image of damage; i.e., more accurate localization with less noise.

In Section 2, the overall methodology for signal processing, image generation and image fusion is explained. Experimental procedures and recorded data are described in Section 3. Results are presented and discussed in Sections 4 and 5, respectively, and concluding remarks are made in Section 6.

2. Methodology

Consider a spatially distributed array of N discrete transducers bonded to a plate at known locations. There are a total of $N(N - 1)$ possible transmit–receiver combinations, which can be reduced by a factor of two due to reciprocity. If the excitation is a typical high voltage spike (fast rise time with a slow decay), then received signals are broadband and usually contain multiple Lamb wave modes. Sets of signals are acquired at different times, and changes in the signals are analyzed to localize any damage that may have occurred between acquisitions. The broadband nature of the signals is both desirable and problematic. It is desirable because the multiple frequencies and modes contain more information than a bandlimited, single mode signal, but it is problematic because the various modes travel at different velocities and are dispersive, making it difficult to analyze the residual signals. The analysis steps presented here comprise one practical approach for effectively utilizing broadband Lamb wave data, and consist of signal processing, image generation, and image fusion. Several figures of merit are defined to evaluate the efficacy of the resulting images for localizing damage.

2.1. Signal processing

Lamb waves generated by a circular piezoelectric transducer using a broadband excitation are typically multi-modal, where the modes present are a function of the plate thickness, the transducers properties, and

the bandwidth. The fundamental symmetric (S_0) and antisymmetric (A_0) modes dominate at lower frequencies since they are the only modes that can exist below the A_1 mode cutoff frequency. If signals are low pass filtered to remove all components above the A_1 cutoff frequency, then only the S_0 and A_0 modes will remain. If signals are additionally band pass filtered, then either the A_0 or S_0 mode may dominate depending upon the relative excitability of each mode for the specific transducer and plate geometry.

Consider a set of $N_p = N(N-1)/2$ signals from the N transducers. Each signal is digitally filtered by convolution with a family of three cycle, Hanning-windowed tone bursts at frequencies of (f_1, f_2, \dots, f_M) ; one set of raw signals yields M sets of filtered signals. The set at each center frequency f_m can then be analyzed to determine the group velocity for that frequency based upon a linear fit of experimentally determined arrival times versus measured transducer-to-transducer distances. The arrival times are determined from the time of the peak of the envelope of the first direct arrival, which is typically the faster S_0 mode unless the A_0 mode is strongly dominant.

Due to differences in both transducers and bonding, signal amplitudes are not necessarily consistent for all of the transducer pairs. Thus, they are scaled based upon the separation distances and the measured amplitudes of the direct arrivals for each filter frequency. Let $(a_1^m, a_2^m, \dots, a_{N_p}^m)$ be the amplitudes of the direct arrivals for the N_p transducer pairs and the m th filter, and let $(d_1, d_2, \dots, d_{N_p})$ be the corresponding transducer-to-transducer distances. The signals are normalized so that the amplitude of the direct arrival for the first transducer pair is unity, and the others are scaled appropriately to reflect the $1/\sqrt{R}$ decay in amplitude with distance,

$$\hat{v}_i^m(t) = \frac{v_i^m(t)}{a_i^m} \sqrt{\frac{d_1}{d_i}}. \quad (1)$$

Here v_i^m and \hat{v}_i^m are the raw and scaled signals, respectively, from the i th transducer pair and the m th filter.

The final signal processing step is to subtract a baseline signal recorded from the undamaged plate from the current signal of interest. These residual signals, which are very small if there are no changes in the structure, contain information about any damage that may have occurred in the interval between the acquisitions.

2.2. Image generation

Individual images at each filter frequency f_m are generated by shifting and adding the residual signals according to an appropriate time shifting rule. Consider the i th transducer pair with the transmitter located at coordinates (x_i^t, y_i^t) and the receiver located at (x_i^r, y_i^r) . If there is a scatterer located at (x, y) , then the time for a wave to travel from the transmitter to the scatterer and back to the receiver is

$$t_i^{xy} = \frac{\sqrt{(x_i^t - x)^2 + (y_i^t - y)^2} + \sqrt{(x_i^r - x)^2 + (y_i^r - y)^2}}{c_g}, \quad (2)$$

where c_g is the group velocity. Each residual signal $r_i^m(t)$ is then shifted by t_i^{xy} , and all shifted signals are summed to yield the averaged signal at (x, y) ,

$$s_m(t; x, y) = \frac{1}{N_p} \sum_{i=1}^{N_p} r_i^m(t - t_i^{xy}) w(t - t_i^{xy}). \quad (3)$$

Here $r_i^m(t)$ is the residual signal for filter m and transducer pair i , and $w(t)$ is a windowing function. The resulting image value at the point (x, y) is given by

$$E_m(x, y) = \int_{T_1}^{T_2} [s_m(t; x, y)]^2 dt. \quad (4)$$

The time origin for the integrand of Eq. (4) is the nominal arrival time for location (x, y) , and T_1 and T_2 are set to ensure that the range of integration is centered on the scattered echoes when (x, y) is an actual flaw location. If there is only one transducer pair, then the image consists of concentric ellipses, with ellipses corresponding to echoes. As additional transducer pairs are accumulated, signals reinforce where multiple ellipses intersect

and signals are in phase, and destructively interfere or average out elsewhere. This computation is performed at each point on a grid encompassing the desired area over which the image is formed, and is repeated for each frequency. The result is a set of M images, each one corresponding to one of the filter frequencies f_m .

2.3. Image fusion

Image fusion refers to the combining, or fusing, of the multiple images with the overall goal of obtaining an improved image; i.e., a better signal-to-noise ratio and more accurate localization of damage. Individual images contain unwanted features (i.e., noise) resulting from three primary causes: (1) phasing artifacts, (2) extra signal artifacts, and (3) signal alignment and distortion artifacts. Phasing artifacts occur when multiple cycles from the same echoes are alternately in and out of phase in a spatial neighborhood. Extra signal artifacts result from waves reflecting from boundaries after scattering by damage, unwanted modes generated by the transducer scattering from damage, or the desired mode converting to an unwanted mode by the damage. Signal alignment and distortion artifacts occur when the two signals being subtracted do not perfectly match for reasons other than damage (e.g., temperature changes, surface variations, etc.). Since different frequencies and modes travel at different wave speeds, have different wavelengths, and may interact differently with flaws and geometry, a particular artifact may appear at different locations on the individual images, or be absent completely from some images. If the dominant response from damage occurs at the same location, it is feasible to combine images to reduce artifacts and preserve damage indications.

Images are fused by considering one pixel at a time, and determining the pixel value of the fused image from the corresponding pixels of the individual images; neighboring pixels are not considered. Several different strategies for image fusion are possible. If the goal is to reduce noise, then averaging the individual pixel values would be appropriate. Averaging may also be helpful in reducing the amplitude of artifacts, particularly if an artifact is only present in a few of the images of a fairly large set. However, the fusion process that is most effective in reducing artifacts is to take the minimum pixel value; i.e., the pixel value of the fused image is the minimum value of all the corresponding pixels of the individual images. This is the algorithm implemented here. A potential risk of using this method is that if an indication from actual damage is missing from one of the individual images, it will also be missing from the fused image. The risk could be mitigated by, for example, discarding the minimum value if it is an outlier, although such modifications were not considered here. This possible problem could be exacerbated if scattering from damage is directional and not all transducer pairs receive scattered signals, as would be the case for a crack. However, the sparse array geometry somewhat mitigates the directionality issue because, even for a directional scatterer, the majority of the pairs will be oriented to receive a non-zero scattered signal.

2.4. Figures of merit

How well an image localizes damage can be quantified by both the location error and the background noise level. The location error is simply the distance between the actual location of damage and the location of the peak value on the image. The image is then divided into two regions: (1) the damage circle, which is a circle of diameter 25 mm centered at the peak location, and (2) the image background, which is the remainder of the image (i.e., the damage circle is excluded). The background noise can be quantified by two values: the peak value and the 95% noise threshold. The background peak value (outside of the damage circle) is normalized by the peak value within the damage circle. The 95% noise threshold is the threshold level below which 95% of the background data falls; it is also normalized by the peak value within the damage circle. The range of possible values for both background parameters is 0–1.

3. Experiments

A 6061 aluminum plate of dimensions 610 mm × 610 mm × 4.76 mm was instrumented with four piezoelectric transducers as summarized in Table 1. The transducers were constructed from 12.5 mm diameter PZT disks backed with epoxy, and were bonded to the plate surface with conductive epoxy. The transducers were driven using a commercial pulser receiver with spike mode excitation, and received signals were bandpass

Table 1

Transducer locations for 610 mm × 610 mm Aluminum plate

Description	<i>X</i> coordinate (mm)	<i>Y</i> coordinate (mm)
Transducer #1	184	337
Transducer #2	379	413
Transducer #3	454	225
Transducer #4	264	148

filtered from approximately 50 kHz to 1 MHz prior to digitization. Each measurement set consisted of the through transmission signals acquired from the six transducer pairs. The sampling frequency was 50 MHz, and a window of 500 μ s was acquired, which corresponds to approximately four transits of the plate by the S_0 mode.

The cutoff frequency for the A_1 mode is approximately 330 kHz, and the frequency range of interest for these experiments extends from 140 to 330 kHz. The S_0 mode is dominant because the transducer diameter matches the half-wavelength of the S_0 mode at approximately 220 MHz, whereas the A_0 mode has a null at about 180 MHz where the transducer diameter matches a full-wavelength [23]. Observations of the direct arrivals showed only very small amplitude A_0 arrivals, less than 10% of the S_0 amplitudes.

Damage was introduced in the form of three through holes; their locations and diameters are summarized in Table 2. Signals were recorded from before and after each hole was drilled, and it was estimated that any temperature variations during the measurement process were less than $\pm 2^\circ\text{C}$.

4. Results

Signals were filtered by convolution with 20 different 3-cycle tone bursts with frequencies ranging from 140 to 330 kHz in 10 kHz increments. Filtered signals were scaled as per Eq. (1), and signal pairs recorded before and after each hole was drilled were directly subtracted to obtain the residual signals. A variable width rectangular summing window was used with width T_m inversely proportional to frequency f_m to keep the number of cycles within the window constant regardless of frequency. The width was set to 3 μ s at 220 kHz.

A set of 20 single frequency images were generated for each of the three holes as per the imaging algorithm of Section 2.2. Each image was normalized by its maximum value, and the normalized images were fused using the minimum pixel algorithm of Section 2.3. Both individual and cumulative figures of merit were computed. For the cumulative figures of merit, the fusion process began at 140 kHz and images were fused one at a time until all 20 were incorporated.

Due to the large number of images generated, only a few are shown here to illustrate the process. Fig. 1 shows 140 kHz single images computed from signals recorded immediately before and after drilling of hole #2 (3.2 mm in diameter). The color scale is normalized so that dark red corresponds to the peak intensity of the image and dark blue is zero. The large image is of the entire plate, and the two smaller images are zoomed regions of a no-damage location (upper figure) and of the hole location (lower figure). Figs. 2 and 3 are also of hole #2 but with frequencies of 230 and 320 kHz, respectively. For all three figures, the “+” symbols indicate the transducer locations, and the damage circle shown on the lower zoomed image is centered at the peak location of the fused image.

To better understand the images, approximate received signals were computed for the same plate, transducer and flaw geometry based upon a number of simplifying assumptions. It was assumed that the transducers were perfect point sources and point receivers, and that they generated both S_0 and A_0 modes, with the A_0

Table 2

Hole diameters and locations

Description	Diameter (mm)	<i>X</i> coordinate (mm)	<i>Y</i> coordinate (mm)
Hole #1	6.4	297	335
Hole #2	3.2	330	180
Hole #3	6.4	421	378

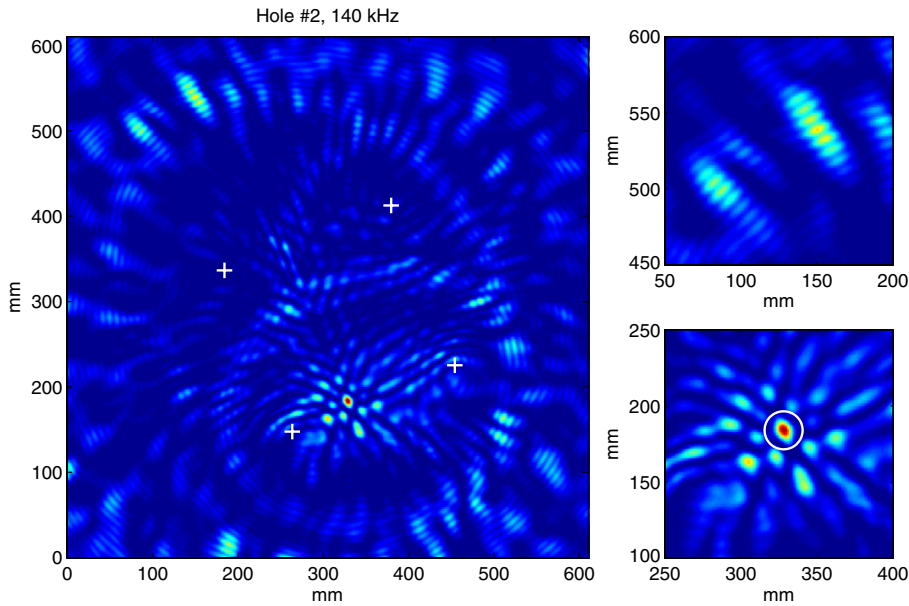


Fig. 1. Single frequency full plate and zoomed images for hole #2 at 140 kHz displayed with a linear color scale. The lower right zoomed image is centered on the actual hole coordinates of (330 mm, 180 mm), and the upper right zoomed image shows typical background noise.

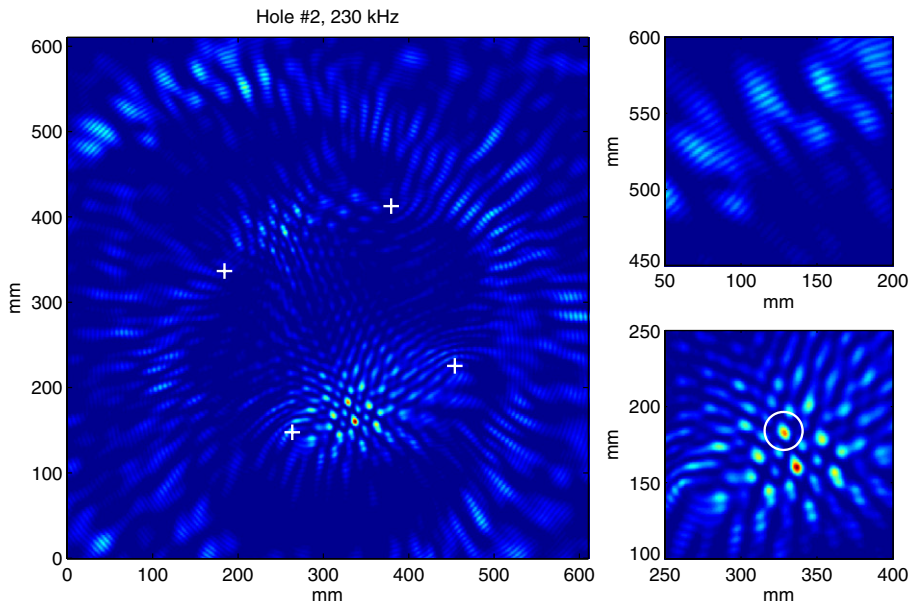


Fig. 2. Single frequency full plate and zoomed images for hole #2 at 230 kHz displayed with a linear color scale (same zoom windows as Fig. 1).

amplitude set to 10% of the S_0 amplitude. It was further assumed that these incident waves were cylindrically scattered from the hole and that all waves were perfectly reflected from the boundaries with no mode conversions or phase shifts. Neglected were both the small effect of the scatterer on the incident wave and the small signals resulting from multiple scattering between the hole and the boundaries, although multiple boundary reflections of the scattered wave were incorporated. It was also assumed that the signals before and after introduction of the hole were perfectly aligned (i.e., the baseline signal was perfectly removed). The source time

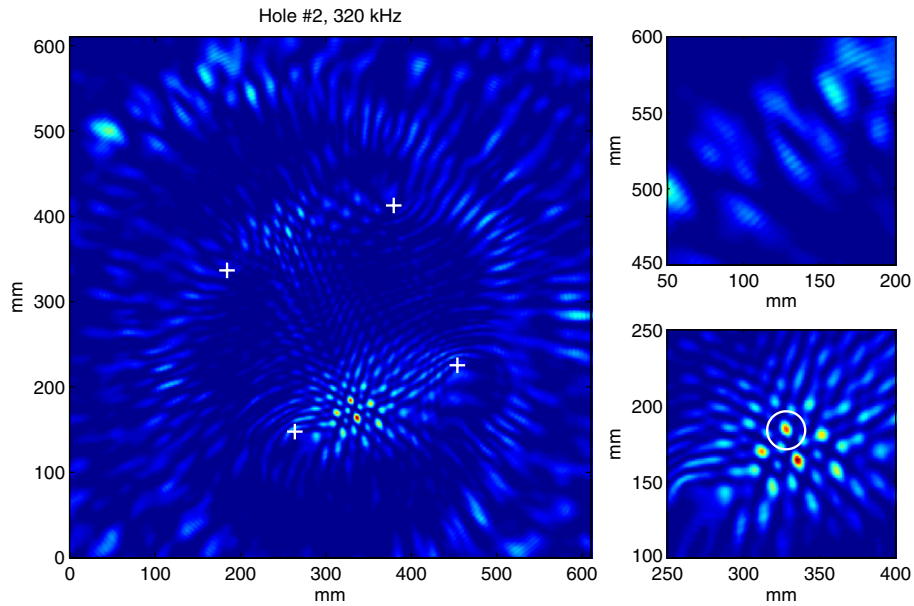


Fig. 3. Single frequency full plate and zoomed images for hole #2 at 320 kHz displayed with a linear color scale (same zoom windows as Fig. 1).

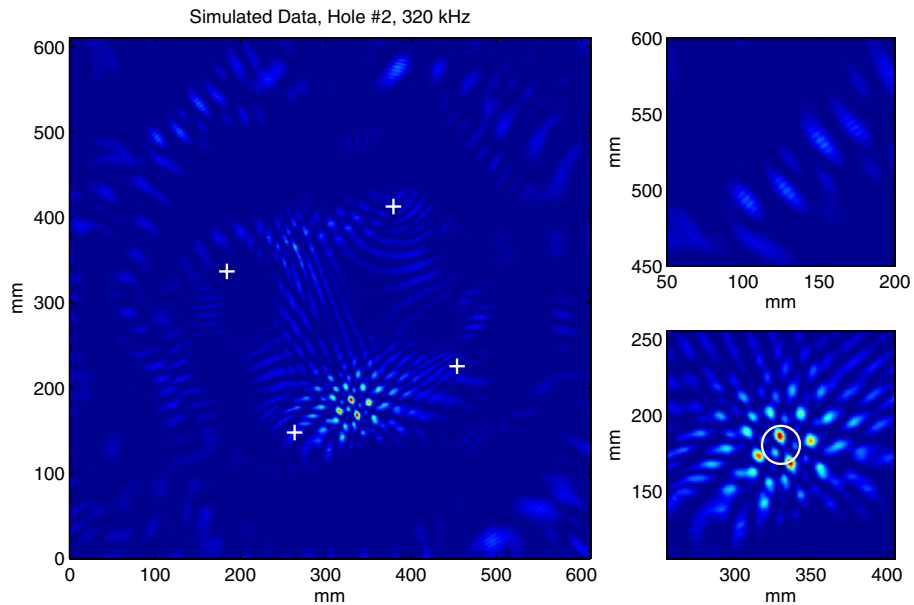


Fig. 4. Single frequency full plate and zoomed images for hole #2 at 320 kHz generated from simulated signals. Images are displayed with a linear color scale and with the same zoom windows as Fig. 1; the circle in the lower right image is centered at the nominal hole location.

function was a three cycle tone burst for both modes, which were then propagated according to their respective dispersion curves [24,25]; boundary reflections were incorporated via the method of images. These simulated signals were processed identically to the experimental data, except that the filter kernels consisted of five cycles instead of three to better match the experimental results. Fig. 4 shows images at 320 kHz, which correspond to those of Fig. 3. The phasing artifacts in the vicinity of the hole are remarkably similar. The

background noise further away from the hole is qualitatively similar to the experimental data, although the amplitude is substantially less and the details are different.

Fig. 5 shows images of hole #2 after the 20 single frequency images are fused, and results for all three holes are summarized in Table 3 and Fig. 6. In the table, the minimum, maximum and mean values for the figures of merit refer to the 20 individual images. Fig. 6 shows individual and cumulative background peak value and noise ceiling results for the three holes. The individual values are those for each single frequency image, and the cumulative values are the fusion results as each individual image is incorporated, beginning at 140 kHz and progressing in ascending frequency order.

5. Discussion of results

The images of Figs. 1–3 illustrate typical characteristics of images generated from a spatially distributed array. First, there is a distinctive pattern of artifacts in the vicinity of the actual hole location, where the positions and spacing of the artifacts vary with frequency. These artifacts result from constructive and destructive interference of multiple cycles of the scattered signals, and are a consequence of the limited bandwidth. A broader bandwidth does not appreciably improve these artifacts because of both dispersion and the preferred excitability of specific frequencies. For the data shown here, even though the excitation was broadband, the S_0 mode at approximately 230 kHz is dominant and images generated from unfiltered signals are very similar to those from the 230 kHz filtered signals. Second, there are additional artifacts that are more spatially distributed and appear to roughly follow curved trajectories. Since these artifacts are much less obvious in the images constructed from simulated signals, they are most likely caused by a combination of signal-baseline misalignment, perturbation of the outgoing wave by the hole, and multiple scattering of boundary reflections from the hole. All three of these sources of artifacts wholly or partially result from boundary reflections, and since different frequencies have different propagation velocities, reflection coefficients and wavelengths, these artifacts are also a function of frequency.

When there is a large misalignment between the signal and the baseline, such as is the case for a significant temperature difference, the initial arrivals are no longer perfectly aligned in time and there are significant echoes in the residual signals at the time of the direct arrival. These initial echoes result in artifacts that tend to be

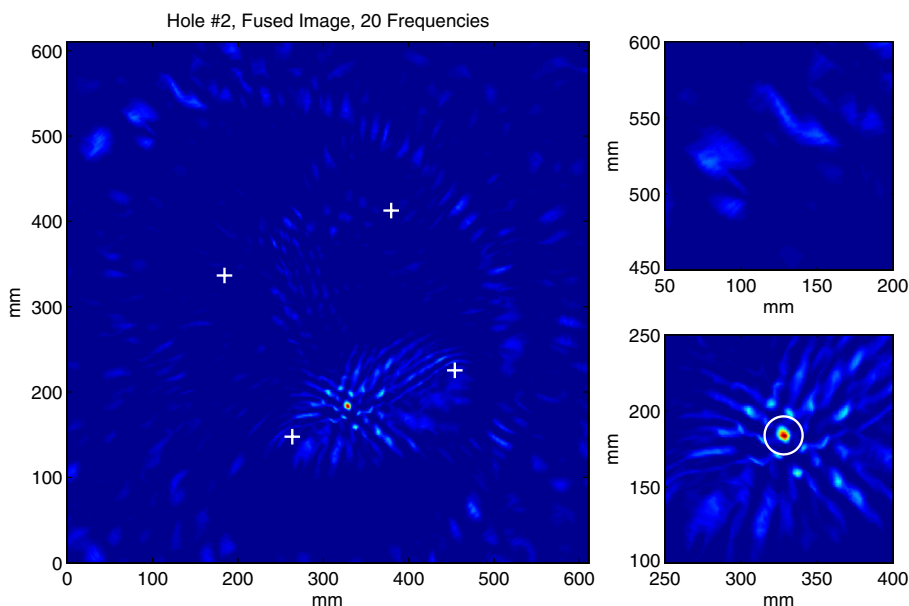


Fig. 5. Fused full plate and zoomed images for hole #2 displayed with a linear color scale (same zoom windows as Fig. 1).

Table 3
Summary of image fusion results

	Figure of merit	Minimum	Maximum	Mean	Fused
Hole #1	Location error	1.0 mm	22.9 mm	3.1 mm	2.3 mm
	Background peak	0.74	1.00	0.89	0.61
	95% Noise threshold	0.13	0.20	0.16	0.07
Hole #2	Location error	3.1 mm	23.2 mm	15.3 mm	4.4 mm
	Background peak	0.68	1.00	0.94	0.49
	95% Noise threshold	0.13	0.20	0.16	0.07
Hole #3	Location error	6.9 mm	27.6 mm	13.1 mm	11.0 mm
	Background peak	0.69	1.00	0.93	0.57
	95% Noise threshold	0.15	0.22	0.17	0.08

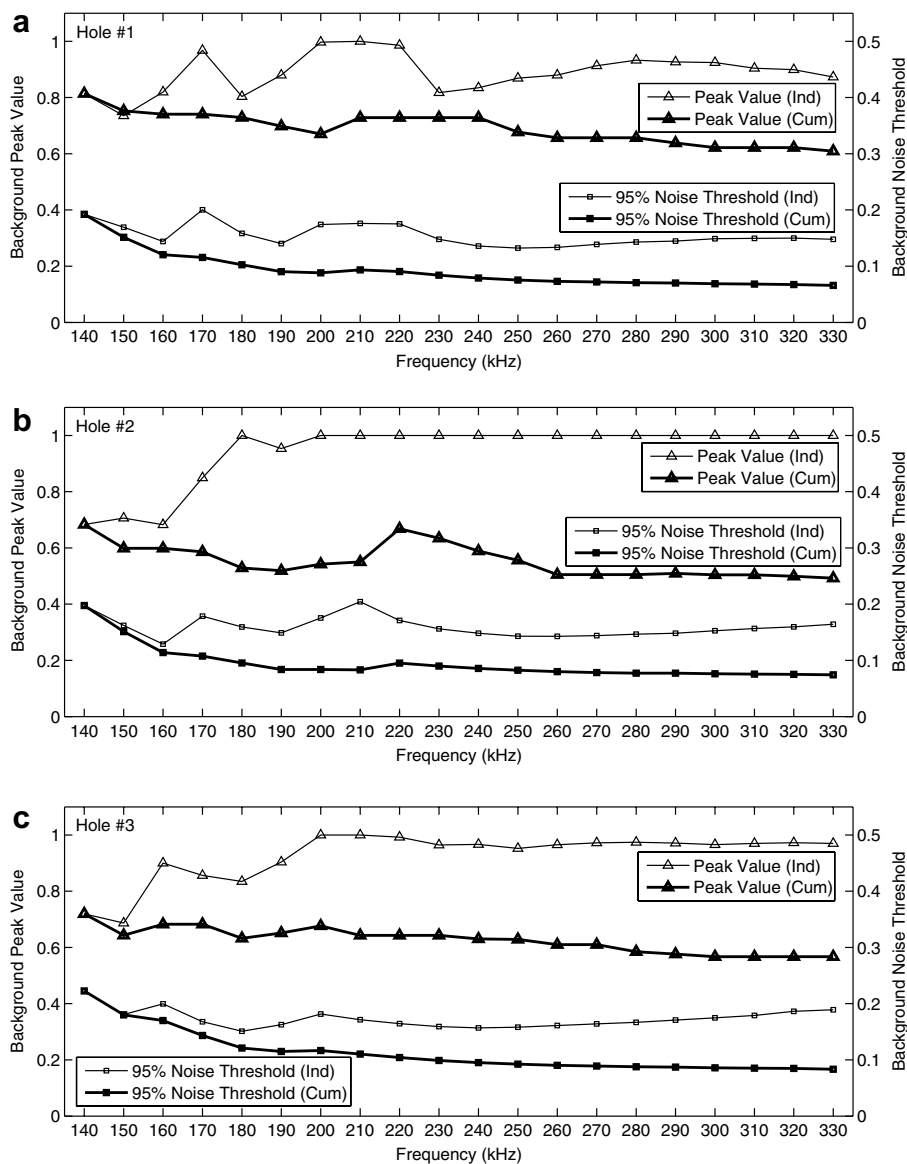


Fig. 6. Individual and cumulative background statistics for the fused images of (a) hole #1, (b) hole #2, and (c) hole #3.

concentrated at the transducer locations, particularly when these direct residual echoes are large in amplitude compared to echoes scattered from damage.

The fused images of Fig. 5 clearly have fewer and lower amplitude artifacts compared to the individual images of Figs. 1–3. This improvement is the direct result of the various artifacts changing in location with frequency, and the main response from damage remaining at the same location.

Referring to Table 3, even the worst case location errors from individual images are less than 30 mm, showing that single frequency images are reasonably effective in locating damage. The fusion process considerably reduces the location errors with all holes being unambiguously located very close to their actual positions. The average location error for the three holes is 5.9 mm with the largest location error corresponding to the one hole (hole #3) that was outside of the transducer bounding box. The background noise statistics also showed considerable improvement after image fusion. For many of the individual images, one or more of the phasing artifacts was larger in amplitude than the main damage peak, as evidenced by a maximum background peak of 1. The fused images all had background peak levels of approximately 0.5–0.6, and the background noise ceiling was lowered by a factor of 2–3 compared to the individual images. The plots of Fig. 6 more clearly show the damage localization ability of the individual images as well as the efficacy of the fusion process. Even though the lower frequency images perform better in terms of the background peak value, the higher frequency images still contribute significantly to the overall reduction in background noise of the fused image.

6. Summary and conclusions

In this paper a method of utilizing information from multiple frequencies has been proposed and implemented for improving the quality of images constructed from sparse transducer arrays attached to plate-like structures. It has been demonstrated on a 4.76 mm thick aluminum plate from which broadband signals were obtained from glued-on piezoelectric discs. Results show the overall efficacy of the imaging process using only four transducers, and also indicate that damage can be better localized and background noise significantly reduced by fusing images generated from applying bandpass filters at various frequencies.

Although results are quite good for data presented here, which was obtained under nominal laboratory conditions, several issues should be addressed before application of this methodology. One issue is that real damage could be removed from fused images if it is absent from one or more of the individual images. Improved fusion strategies could be implemented to better recognize and mitigate this situation by considering the statistics of the data at each pixel (e.g., remove outliers prior to fusion). A closely related issue is that of poor image registration. If the data are all from the same physical transducers, as was the case here, this problem can most likely be avoided, but if multiple images are acquired from two or more transducer arrays, poor image registration may result. A third issue is that of dispersion. Here we have minimized dispersion by bandpass filtering and selecting frequencies where dispersion is not severe. If dispersion curves are known, then dispersion compensation methods could be employed [25]. An alternate approach is to use envelope detected signals for the imaging at the expense of poorer localization [18]. A fourth issue is signal instability, particularly that caused by environmental variations [19]. Methods to compensate signals for these changes are very much needed, although some progress has been made for temperature variations [26,27]. Finally, the effect of the type, orientation and location of damage on the imaging process needs to be investigated, both numerically and experimentally, as well as the effect of damage at multiple locations. Even though these are challenging implementation issues, the results presented here are significant because they demonstrate that systematic incorporation of multi-frequency information can significantly improve the detection and localization of damage.

Acknowledgements

This work was partially supported by NSF Contract Number ECS-0401213. The authors thank Yinghui Lu for assisting with the measurements, and the anonymous reviewers for their helpful comments and suggestions.

References

- [1] D.A. Alleyne, P. Cawley, The interaction of Lamb waves with defects, *IEEE Trans. Ultrason. Ferroelectr. Freq. Control* 39 (1992) 381–397.
- [2] T. Ghosh, T. Kundu, P. Karpur, Efficient use of Lamb modes for detecting defects in large plates, *Ultrasonics* 36 (7) (1998) 791–801.
- [3] P. Fromme, M.B. Sayir, Detection of cracks at rivet holes using guided waves, *Ultrasonics* 40 (1–8) (2002) 199–203.
- [4] Z. Chang, A. Mal, Scattering of Lamb waves from a rivet hole with edge cracks, *Mech. Mater.* 31 (3) (1999) 197–204.
- [5] J.L. Rose, Guided wave nuances for ultrasonic nondestructive evaluation, *IEEE Trans. Ultrason. Ferroelectr. Freq. Control* 47 (2000) 575–583.
- [6] J.L. Rose, D. Jiao, J. Spanner Jr., Ultrasonic guided wave NDE for piping, *Mater. Eval.* 54 (11) (1996) 1310–1313.
- [7] P. Cawley, M.J.S. Lowe, D.N. Alleyne, B. Pavlakovic, P. Wilcox, Practical long range guided wave testing: applications to pipes and rails, *Mater. Eval.* 61 (1) (2003) 66–74.
- [8] J. Li, J.L. Rose, Natural beam focusing of non-axisymmetric guided waves in large-diameter pipes, *Ultrasonics* 44 (2006) 35–45.
- [9] J.-B. Ihn, F.-K. Chang, Detection and monitoring of hidden fatigue crack growth using a built-in piezoelectric sensor/actuator network: I. Diagnosis, *Smart Mater. Struct.* 13 (2004) 315–423.
- [10] V. Giurgiutiu, A.N. Zagari, Characterization of piezoelectric active wafer sensors, *J. Intell. Mater. Syst. Struct.* 11 (2000) 959–975.
- [11] V. Giurgiutiu, J. Bao, Embedded-ultrasonics structural radar for in situ structural health monitoring of thin-wall structures, *Struct. Health Monit.* 3 (2) (2004) 121–140.
- [12] A.S. Purekar, D.J. Pines, S. Sundararaman, D.E. Adams, Directional piezoelectric phased array filters for detecting damage in isotropic plates, *Smart Mater. Struct.* 13 (2004) 838–850.
- [13] P. Wilcox, Omni-directional guided wave transducer arrays for the rapid inspection of large areas of plate structures, *IEEE Trans. Ultrason. Ferroelectr. Freq. Control* 50 (6) (2003) 699–709.
- [14] E. Malyarenko, M. Hinders, Fan beam and double crosshole Lamb wave tomography for mapping flaws in aging aircraft structures, *J. Acoust. Soc. Am.* 108 (4) (2000) 1631–1639.
- [15] E. Malyarenko, M. Hinders, Ultrasonic Lamb wave diffraction tomography, *Ultrasonics* 39 (2001) 269–281.
- [16] K. Leonard, E. Malyarenko, M. Hinders, Ultrasonic Lamb wave tomography, *Inverse Probl.* 18 (2002) 1795–1808.
- [17] C. Wang, J.T. Rose, F.-K. Chang, A synthetic time-reversal imaging method for structural health monitoring, *Smart Mater. Struct.* 13 (2004) 415–423.
- [18] J.E. Michaels, T.E. Michaels, Enhanced differential methods for guided wave phased array imaging using spatially distributed piezoelectric transducers, in: D.O. Thompson, D.E. Chimenti (Eds.), *Review of Progress in Quantitative Nondestructive Evaluation*, vol. 25B, American Institute of Physics, New York, 2006, pp. 837–844.
- [19] G. Konstantinidis, B. Drinkwater, P. Wilcox, The long term stability of guided wave structural health monitoring systems, in: D.O. Thompson, D.E. Chimenti (Eds.), *Review of Progress in Quantitative Nondestructive Evaluation*, vol. 25B, American Institute of Physics, New York, 2006, pp. 1702–1709.
- [20] H. Gao, Y. Shi, J.L. Rose, Guided wave tomography on an aircraft wing with leave in place sensors, in: D.O. Thompson, D.E. Chimenti (Eds.), *Review of Progress in Quantitative Nondestructive Evaluation*, vol. 24B, American Institute of Physics, New York, 2005, pp. 1788–1794.
- [21] C. Valle, J.W. Little, Flaw localization using the reassigned spectrogram on laser-generated and detected Lamb waves, *Ultrasonics* 39 (2002) 535–542.
- [22] R. Benz, M. Neithammer, S. Hurlebaus, L.J. Jacobs, Localization of notches with Lamb waves, *J. Acoust. Soc. Am.* 114 (2) (2003) 677–685.
- [23] V. Giurgiutiu, Tuned Lamb wave excitation and detection with piezoelectric wafer active sensors for structural health monitoring, *J. Intell. Mater. Syst. Struct.* 16 (2005) 291–305.
- [24] Available online: <<http://www.imperial.ac.uk/ndt/public/productservice/disperse.htm>, 2006.>
- [25] P.D. Wilcox, A rapid signal processing technique to remove the effect of dispersion from guided wave signals, *IEEE Trans. Ultrason. Ferroelectr. Freq. Control* 50 (4) (2003) 419–427.
- [26] Y. Lu, J.E. Michaels, A methodology for structural health monitoring with diffuse ultrasonic waves in the presence of temperature variations, *Ultrasonics* 43 (2005) 717–731.
- [27] G. Konstantinidis, B. Drinkwater, P. Wilcox, The temperature stability of guided wave structural health monitoring systems, *Smart Mater. Struct.* 15 (2006) 967–976.